ACS OMEGA

http://pubs.acs.org/journal/acsodf

Article

Experimental and Theoretical Investigations of Fe-Doped Hexagonal MnNiGe

S. Shanmukharao Samatham,*,# Akhilesh Kumar Patel, Ashish Kumar Mishra, Alexey V. Lukoyanov, Lyubov N. Gramateeva, Archana Lakhani, Ganesan Vedachalaiyer, and Suresh Krishnawarrier Gopinatha Warrier

Cite This: *ACS Omega* 2022, 7, 18110–18121

Read Online

ACCESS | Metrics & More | Article Recommendations

ABSTRACT: We report a comprehensive investigation of $MnNi_{0.7}Fe_{0.3}Ge$ Heusler alloy to explore its magnetic, caloric, and electrical transport properties. The alloy undergoes a ferromagnetic transition across $T_C \sim 212$ K and a weak-antiferromagnetic transition across $T_t \sim 180$ K followed by a spin-glass transition below $T_f \sim 51.85$ K. A second-order phase transition across T_C with mixed short and long-range magnetic interactions is confirmed through the critical exponent study and universal scaling of magnetic entropy and magnetoresistance. A weak first-order phase transition is evident across T_t from magnetization and specific heat data. The frequency dependent cusp in $\chi_{AC}(T)$ along with the absence of a clear magnetic transition in specific heat $C(T)$ and resistivity $\rho(T)$ establish the spin glass behavior below T_f. Mixed ferromagnetic and antiferromagnetic interactions with dominant ferromagnetic coupling, as revealed by density functional calculations, are experimentally evident from the large positive Weiss temperature, magnetic saturation, and negative magnetic-entropy and magnetoresistance.

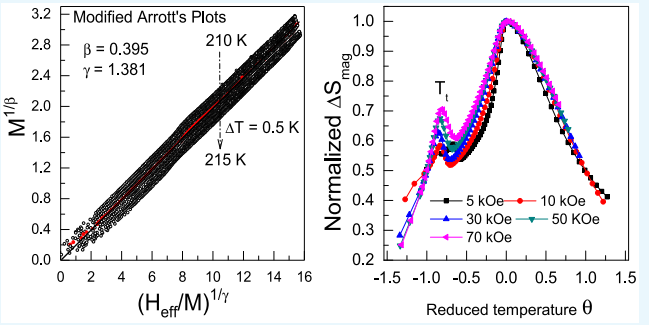

INTRODUCTION

The physics of phase transitions is important to understand the properties of compounds. Exploration of the critical phenomena across the transition temperature unveils the nature of the phase transition. A second-order phase transition (SOPT) from paramagnetic (PM) to ferromagnetic (FM) state is characterized by a continuous variation of the spontaneous magnetization, an order parameter. Nevertheless, the magnetic properties of the compounds are governed by the exchange interactions among the spins. FM compounds with a large change in magnetic entropy and adiabatic temperature T_{ad} (change in temperature of the system under adiabatic condition without exchange of heat) across the transition temperature near room temperature are potential candidates for technological applications such as magnetic refrigeration. In recent times, Heusler compounds have become materials of topical interest for their multifunctional and peculiar properties such as topological insulators,[1,2] Weyl semimetals,[3] spin-gapless semiconductors,[4] shape memory effect,[5,6] half-metals,[7−9] exchange bias, large magnetoresistance, and magnetocaloric effect.[10,11]

Heusler alloys with 1:1:1 stoichiometry have been receiving a great deal of attention due to their tunable magnetic properties with substitution, magnetic field, and hydrostatic pressure. Substitution/disorder driven suppression of a first-order magneto-structural transition in 1:1:1 stoichiometric Heusler alloy MnNiGe was reported.[12,13] It undergoes a structural transition at $T_t = 470$ K from high-temperature Ni_2In-type hexagonal austenite to a TiNiSi-type orthorhombic martensite structure.[14,15] In addition, it is reported to order antiferromagnetically at $T_N^M = 346$ K in the martensitic state, followed by a ferromagnetic phase below $T_C^A = 205$ K. The magnetic properties of MnNiGe have been reported to be substitution and site specific. A gradual replacement of Fe at Mn site, $Mn_{1-x}Fe_xNiGe$, has suppressed T_t down to 84 K at $x = 0.26$. The alloys with $x > 0.26$ crystallize in a Ni_2In-type hexagonal structure with a glassy phase at low temperatures.[12] On the other hand, in $MnNi_{1-x}Fe_xGe$ where Ni is gradually replaced by Fe, the systems remain in the ferromagnetic austenite phase for $x > 0.3$.[12] $MnNi_{0.7}Fe_{0.3}Ge$ is reported to undergo a structural transition at $T_t = 189$ K (below which a small thermal hysteresis was noticed) and austenite ferromag-

Received: March 19, 2022
Accepted: May 5, 2022
Published: May 17, 2022

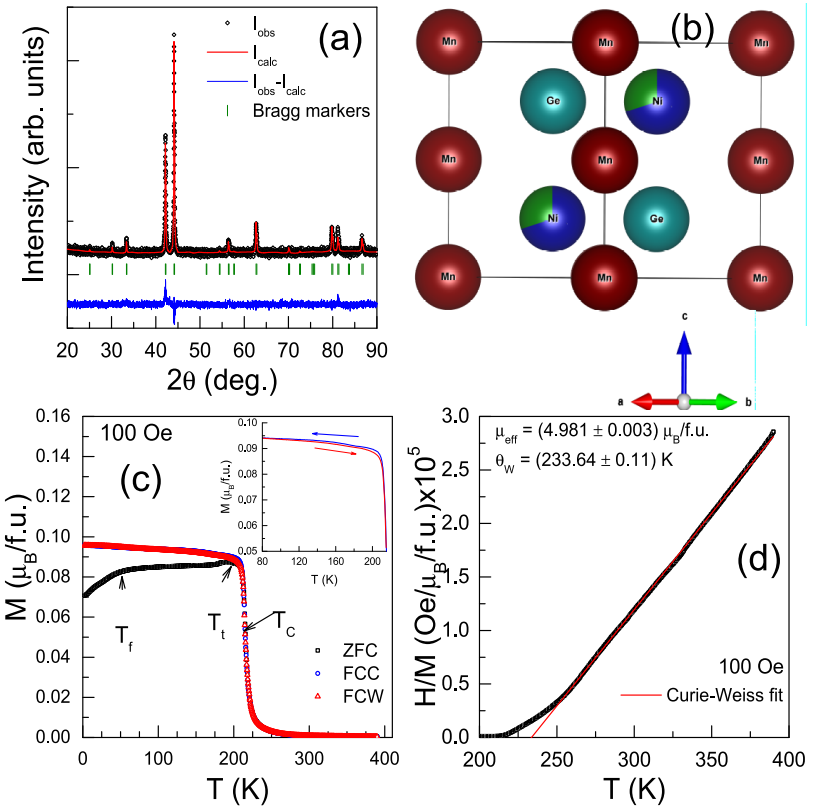

Figure 1. (a) Refined X-ray diffraction pattern of $MnNi_{0.7}Fe_{0.3}Ge$ using the $P6_3/mmc$ space group. The global χ^2 = 2.31 with Bragg factor = 14.6 and RF-factor = 15.2. (b) Crystal structure with lattice parameters $a = b$ = 4.102 Å and c = 5.368 Å. Ni atom shares 30% of its occupancy with Fe. Mn−Mn nearest distance along the c-axis is 2.684 Å. (c) Temperature dependence of magnetization under 100 Oe in ZFC, FCC, and FCW processes. ZFC and FCW curves are separated from each other below T_t = 180 K. Inset: A narrow thermal hysteresis is noticed between FCC and FCW in the temperature range 75−215 K. (d) Curie−Weiss fit of the inverse susceptibility. The Weiss temperature and the effective magnetic moment are found to be (233.64 ± 0.11) K and μ_{eff} = (4.981 ± 0.003) μ_B/f.u., respectively.

netic transition at T_C^A = 211 K.[12] Recently, $MnNi_{0.8}Fe_{0.2}Ge$ has been investigated for its successive magnetic transitions with a field-induced conversion of the low-temperature magnetic state to the FM state.[16] Nevertheless, the universality class of the high-T SOPT and transport behavior of $MnNi_{0.7}Fe_{0.3}Ge$ are unclear.

In the present study, we report on the universality class and critical magnetic behavior of $MnNi_{0.7}Fe_{0.3}Ge$ using the combined results of magnetization and specific heat, combined with ab initio calculations. The study has been focused on understanding the phenomena across T_C^A and T_t. Our results reveal that the alloy crystallizes in a Ni_2In-type hexagonal structure at room temperature and undergoes a second-order phase transition at $T_C \sim$ 212.5 K. A narrow thermal hysteresis below 180 K disappears in a field of ∼5 kOe above which the system behaves ferromagnetically down to 2 K. Mixed (short- and long-range) interactions are suggested by the critical exponents. The Sommerfeld coefficient of electronic specific heat (γ_{el} = 15.9 ± 0.5 J·mol^{-1}.K^{-2}) and electrical resistivity confirm the metallic character. The self-consistency of the critical exponents, extracted using magnetization, is established through the analysis of the magnetocaloric and the magneto-resistance methods. A second-order phase transition across T_C ∼ 212 K is confirmed through universal scaling of the magnetic-entropy and magnetoresistance data. A cluster-glass type behavior with weakly coupled magnetic clusters is reported below 50 K. The dual transitions can be carefully manifested/tuned to achieve a table-like magneto-caloric effect for magnetic refrigeration. The effect of the magnetic field on the electrical resistivity across the magnetic transition temperature can be utilized in magneto-resistive applications.

METHODS

A polycrystalline $MnNi_{0.7}Fe_{0.3}Ge$ has been prepared by the arc-melting method. The constituent elements Mn, Ni, Fe, and Ge (of purity better than 99.999%) were taken in a stoichiometric ratio and were loaded into a copper hearth. The elements were melted under a continuous supply of argon gas. The ingot was melted several times by flipping each time. X-ray diffraction pattern at room temperature is collected on a powder specimen using PANalytic X'Pert Pro X-ray diffractometer with Cu−K_α radiation. Energy-dispersive X-ray (EDAX) spectroscopy measurements (not shown here) were carried out using JSM-7600F. The atomic percentages of Mn, Ni, Fe, and Ge are in good agreement with the originally taken stoichiometric ratio within the experimental error. Magnetization was measured with the help of a commercial superconducting quantum interference device-vibrating sample magnetometer (SQUID-VSM) under zero-field cooling (ZFC), field-cooled cooling (FCC), and field-cooled warming (FCW) conditions. Under ZFC conditions, magnetization was recorded during warming (under the ambiance of required set field) after the sample was cooled to 2 K from 400 K in zero-field. Under FCC conditions, magnetization was recorded while the sample was cooled in a finite magnetic field. Consequently, under FCW conditions, magnetization was

https://doi.org/10.1021/acsomega.2c01571
ACS Omega 2022, 7, 18110−18121

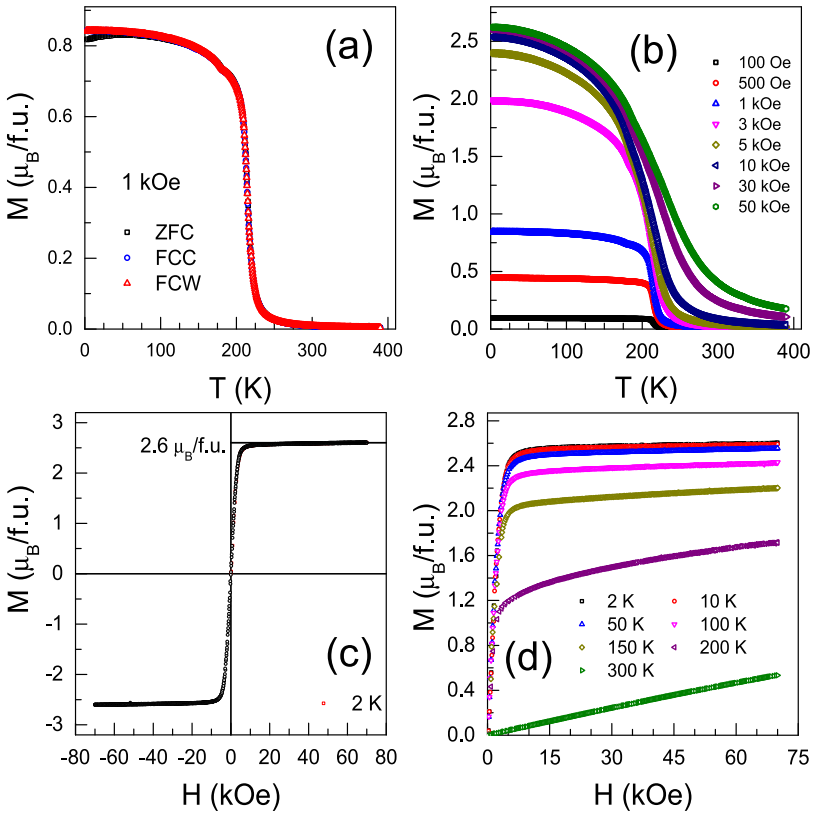

Figure 2. (a) $M(T)$ measured in 1 kOe in ZFC, FCC, and FCW protocols. Reduced bifurcation of ZFC and FCW curves is noticed when compared to 100 Oe. (b) $M(T)$ measured under a few representative magnetic fields. (c) Isothermal magnetization versus field at 2 K. M increases sharply with H with a saturation magnetization of $M_s \sim 2.6$ μ_B/f.u. at a saturation field of $H_s \sim 6.6$ kOe. (d) Isothermal magnetization versus field curves at a few representative temperatures. In the paramagnetic region (at 300 K), M develops linearly with H.

recorded under warming, without switching off magnetic field. Isothermal magnetization versus field curves were measured, under ZFC condition, by ramping the magnetic field. Electrical resistivity was measured using a standard dc-four probe method using a 9 T-Physical Property Measurement System (PPMS). The specific heat was measured using relaxation calorimetry with the help of commercial 14 T PPMS.

The electronic structure was calculated in the Quantum ESPRESSO software[17] using the scalar-relativistic potentials in a local density approximation of Perdew−Zunger-type, included in the standard QE library. Wave functions were decomposed into plane waves, and interactions between ions and valence electrons were taken into account of method of attached plane waves (PAW). To model the concentration of Fe closest to the experiments, we constructed a supercell with 4 f.u. of MnNiGe with 1 Ni ion substituted by Fe that finally resulted in the $MnNi_{0.75}Fe_{0.25}Ge$ composition. For the sufficient convergence in our first-principles calculations, the energy cutoff, i.e., energetic limit, 60 Ry, was taken. A k-mesh of 8 × 8 × 8 k-points was used for the tetrahedron method integration in a reciprocal space.

RESULTS

Figure 1a shows the room-temperature X-ray diffraction pattern of $MnNi_{0.7}Fe_{0.3}Ge$, along with Rietveld refinement using the FullProf suite.[18] The alloy crystallizes in a Ni_2In-type hexagonal structure with the $P6_3/mmc$ space group. The lattice parameters are $a = b = 4.102$ Å and $c = 5.368$ Å. The obtained structure is drawn using visualization for electronic and structure analysis (VESTA),[19] as shown in Figure 1b. Mn occupies the 2a (0, 0, 0) position and Ni/Fe share the 2d (1/3, 2/3, 3/4) positions, while Ge occupies the 2c (1/3, 2/3, 1/4) position. The shortest Mn−Mn distance along the c-axis is 2.6839(1) Å.

The temperature dependence of the magnetization $M(T)$ curve under the influence of 100 Oe is shown in Figure 1c. $M(T)$ rises sharply below 250 K before it takes a down turn around 180 K along with a separation between the ZFC and FCW magnetization curves. In addition, a narrow thermal hysteresis between FCC and FCW is observed in the temperature range 75 to 215 K, as shown in the inset of Figure 1c. Further, $M(T)$ exhibits a down turn below T_f, noted as a freezing temperature. In 100 Oe, the inverse susceptibility $\chi^{-1}(T)$ is fit, as shown in Figure 1d, to the Curie−Weiss law using eq 1

$$\chi(\cong M/H) = C/(T - \theta_W) \quad (1)$$

where C is the Curie−Weiss constant from which the effective magnetic moment is calculated as $\mu_{eff} = \sqrt{3k_BC/N_A}$ (k_B is the Boltzmann constant and N_A is the Avogadro number). Thus, the obtained effective magnetic moment is $\mu_{eff} = 4.981 \pm 0.003$ μ_B/f.u. A positive and large Weiss temperature $\theta_W = (233.64 \pm 0.11)$ K indicates the prevailing ferromagnetic exchange correlations above the transition temperature. $M(T)$ in 1 kOe is shown in Figure 2a. The bifurcation between ZFC and FCW is found to decrease with increasing H. However, the kink at T_t and the thermal hysteresis, observed below 180 K in 100 Oe, shift toward low-temperature with increasing H up to 3 kOe. In $H \geq 5$ kOe, the kink at T_t is smeared out with

https://doi.org/10.1021/acsomega.2c01571
ACS Omega 2022, 7, 18110−18121

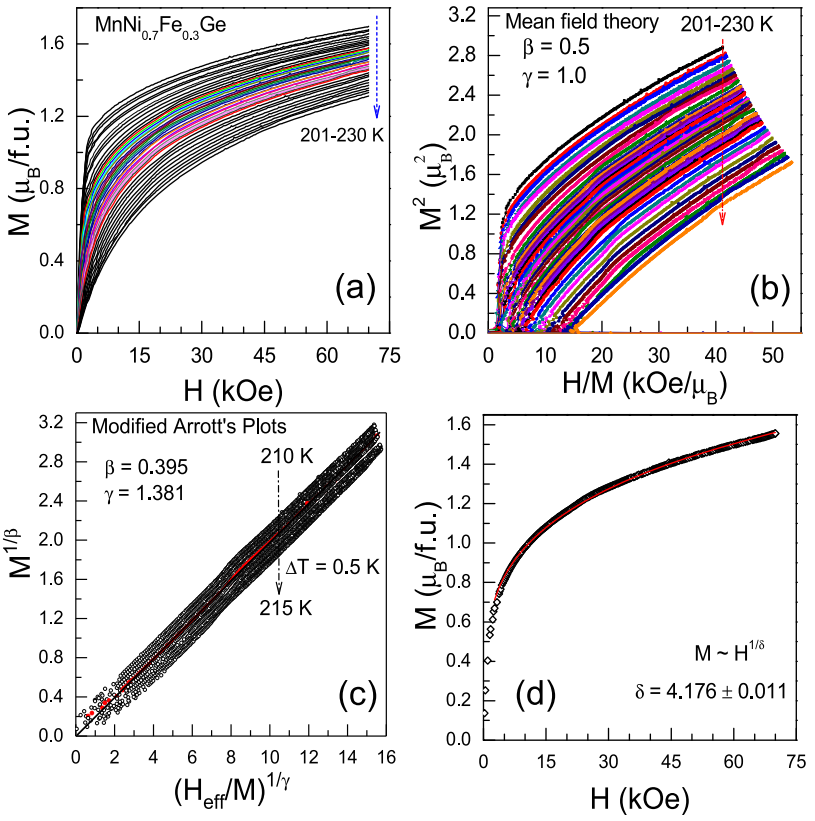

Figure 3. (a) Isothermal magnetization versus curves of $MnNi_{0.7}Fe_{0.3}Ge$ at a few selected temperatures in the temperature range 201−230 K. In particular, $M(H)$ curves are measured with 0.5 K difference in the vicinity of critical transition. (b) Arrott plot M^2 versus H/M with mean-field theory exponents (β = 0.5 and γ = 1). The positive slope of the high-field curves indicate the second order phase transition. (c) Modified Arrott plot $M^{1/\beta}$ versus $(H/M)^{1/\gamma}$ with parallel set of lines with critical exponents β = 0.395 and γ = 1.381. Critical transition isotherm passing through origin is shown in red and the linear fit is shown in dashed lines. (d) $M(H)$ at 212.5 K ($\equiv T_C$), a power-law fit (shown in solid line) using eq 4 yields an exponent δ = 4.176 ± 0.011.

simultaneous vanishing of thermal hysteresis. Such a phenomenon resembles the field-induced weak-AFM to FM transition. Shown in Figure 2b are $M(T)$ curves, measured in constant magnetic fields ranging from 100 Oe to 50 kOe.

Figure 2c shows an isothermal magnetization versus field $M(H)$ up to 70 kOe, recorded at 2 K. $M(H)$ is measured in five quadrants (0 → 70 kOe → 0 kOe → −70 kOe → 0 kOe → 70 kOe). Remnant magnetization M_R is zero, indicative of soft ferromagnetic behavior which is supported by zero coercive field H_c. The saturation magnetization M_s is about 2.6 μ_B/f.u. Figure 2d shows the isothermal $M(H)$ curves, measured at a few selected temperatures. As the temperature is increased, the linearity from the high-field region is extended to low-fields. In the paramagnetic state (at 300 K), M linearly increases with H.

DISCUSSION

Critical Behavior across T_C. In order to understand the magnetism of $MnNi_{0.7}Fe_{0.3}Ge$ i.e. whether localized or itinerant, Rhodes−Wohlfarth (RW) ratio q_c/q_s[20,21] is calculated, where q_c is the number of magnetic carriers per atom and q_s is the saturation magnetic moment. q_s = 2.6 μ_B/f.u. for the present case. q_c = 4.08 μ_B/f.u. is estimated from the effective magnetic moment as $\mu_{eff} = \sqrt{q_c(q_c+2)}$. The RW ratio is obtained as $q_c/q_s > 1$, indicating an itinerant magnetic behavior of the alloy. Further, with an aim of realizing the universality class and the type of magnetic interactions in $MnNi_{0.7}Fe_{0.3}Ge$, a critical study has been carried out with the help of isothermal magnetization curves. A set of $M(H)$ curves were measured in the temperature range 201−209 by 1 K difference, 210−220 by 0.5 K difference, and 221−230 K by 1 K difference, as shown in Figure 3a. In regard to the SOPT from the PM to the FM state, the spontaneous magnetization M_s below the critical transition temperature T_C, the inverse susceptibility χ^{-1} above T_C, and the isothermal magnetization at T_C follow power-laws given by eqs 2, 3, and 4, respectively[22,23]

$$M_s = M_{s0}(t)^{\beta}; \quad T < T_C \tag{2}$$

$$\chi_0^{-1} = \chi_{00}^{-1}(-t)^{\gamma}; \quad T > T_C \tag{3}$$

$$M(H) = DH^{1/\delta}; \quad T = T_C \tag{4}$$

where $t = 1 - T/T_C$ is the reduced temperature and the critical exponents associated with M_s, χ_0, and T_C are β, γ, and δ, respectively, while M_{s0}, χ_{00} ,and D are the critical amplitudes. Arrott plots[24] with mean-field theory exponents (β = 0.5 and γ = 1.0), i.e., M^2 versus H/M, are shown in Figure 3b. In these isotherms, the downward concave curvature of the Arrott plot in high fields hints at SOPT, following Banerjee's criterion.[25] To estimate the correct critical exponents, we have used the modified Arrott plot method (MAP) using Arrott and Noakes magnetic equation of state, eq 5[26]

$$(H/M)^{1/\gamma} = c_1\left(\frac{T - T_C}{T_C}\right) + c_2 M^{1/\beta} \tag{5}$$

https://doi.org/10.1021/acsomega.2c01571
ACS Omega 2022, 7, 18110−18121

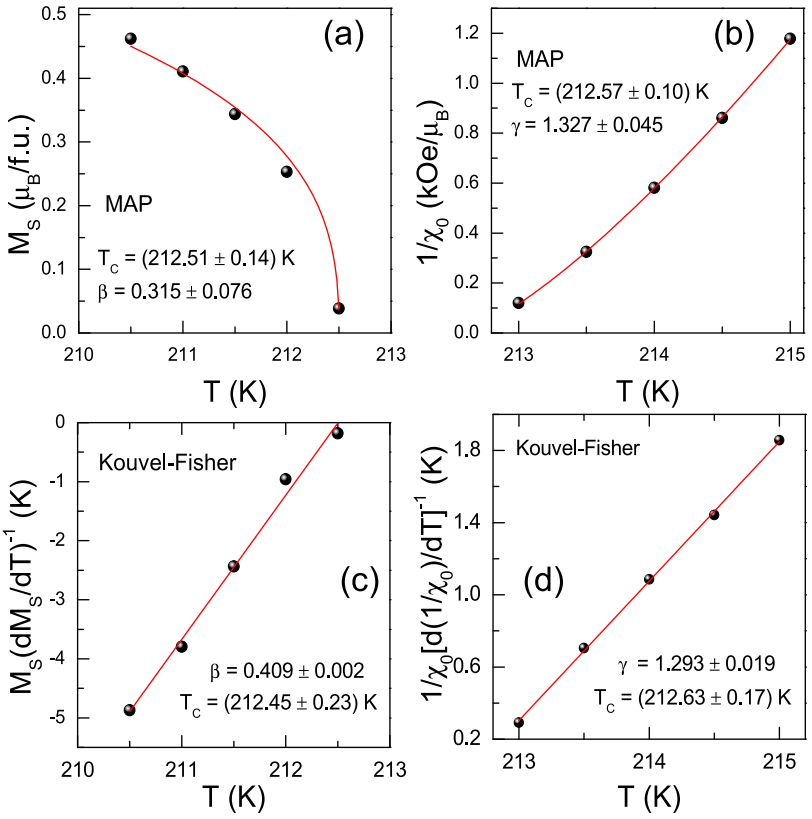

Figure 4. (a) Temperature dependence of spontaneous magnetization M_s. A critical exponent fit of the data using eq 2 produces $\beta = 0.315 \pm 0.076$ and $T_C = (212.51 \pm 0.14)$ K. (b) Inverse susceptibility $1/\chi_0(T)$. $\gamma = 1.327 \pm 0.10$ and $T_C = (212.57 \pm 0.045)$ K are obtained by fitting the data using eq 3. (c) Kouvel–Fisher plot of $M_s(T)$ yielding the exponent $\beta = 0.409 \pm 0.002$ and critical temperature $T_C = (212.45 \pm 0.23)$ K. (d) Kouvel-Fisher fit of $1/\chi_0(T)$ with $\gamma = 1.293 \pm 0.019$ and $T_C = (212.63 \pm 0.17)$ K.

where c_1 and c_2 are constants. Different universal magnetic behaviors such as 3D-Heisenberg ($\beta = 0.365$, $\gamma = 1.386$), 3D-Ising model ($\beta = 0.325$, $\gamma = 1.24$),[27] and tricritical mean field theory ($\beta = 0.25$, $\gamma = 1.0$)[28] were tested by plottng $M^{1/\beta}$ versus $(H/M)^{1/\gamma}$ curves (not shown here).

Various trials were made to obtain the correct critical exponents by taking initial values of $\beta = 0.365$ and $\gamma = 1.386$. $M(H)$ curves were subjected to the demagnetization correction $H_{eff} = H_{applied} - N_D M$. Every time, the newly obtained exponents are validated for the sufficient condition using eq 5 and checked that the modified isotherm of transition temperature passes through the origin ($M^{1/\beta} = 0$, $(H/M)^{1/\gamma} = 0$). After a rigorous exercise, a set of parallel isotherms were obtained, satisfying eq 5 with $\beta = 0.395$ and $\gamma = 1.381$, for which $M^{1/\beta}$ versus $(H/M)^{1/\gamma}$ curves are shown in Figure 3c. M_s and χ_{00}^{-1} are extracted from the intercepts of the $M^{1/\beta}$ and $(H/M)^{1/\gamma}$ axis, respectively. Thus, obtained $M_s(T)$ and $\chi_{00}^{-1}(T)$, shown in Figure 4a,b, are fit using the respective eqs 2 and 3. The obtained critical exponents and transition temperatures through the MAP method are $T_C = (212.51 \pm 0.14)$ K and $\beta = 0.315 \pm 0.076$; $T_C = (212.57 \pm 0.10)$ K, $\gamma = 1.327 \pm 0.045$. Further, more accurate exponents are obtained through the Kouvel–Fisher (KF) method. The plots of $M_s[1/(dM_s/dT)]$ and $\chi^{-1}[1/(d\chi^{-1}/dT)]$ as a function of temperature are shown in Figure 4c,d. The inverse slopes of the linearly fit curves give the exponents $\beta = 0.409 \pm 0.002$ and $\gamma = 1.293 \pm 0.019$ with critical temperatures $T_C = (212.45 \pm 0.23)$ K and $T_C = (212.63 \pm 0.17)$ K, respectively. Using Widom's relation,[29,30] $\delta = 1 + \gamma/\beta$, the estimated δ values through MAP and KF methods are $\delta = 5.212 \pm 1.162$ and 4.161 ± 0.062, respectively, which are in good agreement with δ ($= 4.176 \pm 0.011$) directly obtained through the critical isotherm fit using eq 4, as shown in Figure 3d. The critical exponents do not straight away indicate a single universality class but closely resemble 3D-Heisenberg and 3D-Ising models. The exchange interaction $J(r)$, where r is the distance of interaction, depends on the spatial dimensionality d and the length of interaction σ through a relation $J(r) \sim r^{-(\sigma+d)}$. σ can be calculated from γ using eq 6[31]

$$\gamma = 1 + \frac{4}{d}\left(\frac{n+2}{n+8}\right)\Delta\sigma + \frac{8(n+2)(n-4)}{d^2(n+8)^2}\left[1 + \frac{2G(d/2)(7n+20)}{(n-4)(n+8)}\right](\Delta\sigma)^2 \quad (6)$$

where $\Delta\sigma = (\sigma - d/2)$ and $G(d/2) = 3 - (d^2/16)$. For the present compound, with $d = 3$, $\sigma \sim 1.75$ is obtained and exchange interaction varies as $J(r) \sim r^{-4.75}$ which falls in between the ranges for Mean-field model ($r^{-4.5}$, $\sigma \leq 3/2$) and 3D Heisenberg model (r^{-5}, $\sigma \geq 2$). This indicates the mixed exchange interactions of long-range and short-range $MnNi_{0.7}Fe_{0.3}Ge$. Nevertheless, the closeness of the critical exponents to other models 3D-Ising or 3D-XY point out anisotropic exchange interactions. On the other hand, Pinninti et al. reported a single magnetic transition and 3D-Heisenberg universality with short-range magnetic interactions in $MnCo_{0.7}Fe_{0.3}Ge$[32] and enhancement of transition temperature with Fe substitution in $Mn_{0.7}Fe_{0.3}Co_{0.7}Fe_{0.3}Ge$.[33]

https://doi.org/10.1021/acsomega.2c01571
ACS Omega 2022, 7, 18110−18121

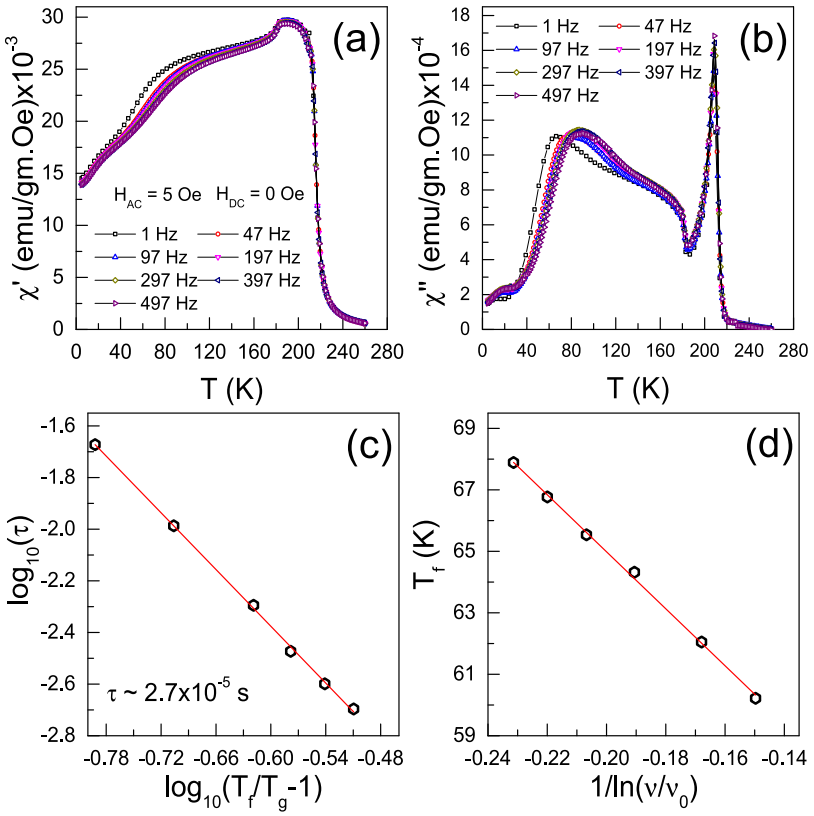

Figure 5. (a, b) χ_{AC}' and χ_{AC}'' measured in labeled frequencies under H_{AC} = 5 Oe and H_{DC} = 0 Oe. The curves show a peak at 213 K along with a hump around 180 K. Below about 52 K, dispersion in χ_{AC}' with a shift in T_f toward high-T. (c) Fit of critical dynamical slowing in relation to $T_f(\nu)$ which gives a relaxation time $\tau_0 \sim 2.7\times 10^{-5}$ s. (d) Fit of Vogel−Fulcher law which yields a characteristic temperature T_0 = (46.45 ± 0.36) K and E_a/k_B = (92.71 ± 1.82) K.

Spin-Glass Behavior below 52 K. Real (χ') and imaginary parts (χ'') of AC-susceptibility χ_{AC} are shown in parts a and b, respectively, of Figure 5. The measurements were carried out in an AC-drive field of H_{AC} = 5 Oe and H_{DC} = 0 Oe under the effect of a few selected frequencies ν = 1, 47, 97, 197, 297, 397, and 497 Hz. The temperature variation of $d\chi'/dT$ (not shown here) exhibits a dip around 213 K, followed by a peak around 180 K, which are in good agreement with T_C and T_t. The dip around 213 K is found to be frequency independent, indicating the long-range magnetic order. However, a dispersion in $\chi'(T)$ is visible below T_t. In ν = 1 Hz, $d\chi'/dT$ exhibits a peak around the freezing temperature T_f ∼ 51.85 K which shifts toward high temperatures with increasing frequency, indicating short-range correlations among the spins. In order to understand these short-range correlations, Mydosh parameter which represents the relative shift of a freezing temperature is estimated as $\phi = \Delta T_f/T_f\Delta[\log_{10}\nu]$ where $\Delta T_f = (T_f)_{\nu_2} - (T_f)_{\nu_1}$ and $\Delta[\log_{10}\nu] = \log_{10}\nu_2 - \log_{10}\nu_1$, with ν_1 = 1 Hz and ν_2 = 497 Hz. For the present compound $\phi \sim 0.12$, which is larger than ϕ reported for cluster spin-glasses and matches with ϕ reported for superparamagnetic systems ($\phi \in [0.10, 0.13]$).[34] Further, relaxation time is obtained with the help of relation between T_f and ν for the dynamical slowing down of spin fluctuations[34,35] above the glass transition temperature of a spin glass, i.e., $\tau = \tau_0(T_f/T_g - 1)^{z\nu'}$, where $\tau = 1/\nu$, τ_0 is the single spin-flip relaxation time, and $z\nu'$ is an exponent. Figure 5c shows a linear fit of $\log_{10}\tau = \log_{10}\tau_0 - z\nu'\log_{10}(T_f/T_g - 1)$. The currently obtained value of $z\nu'$ (= 3.67 ± 0.05) is close to that reported for spin-glass systems.[34] However, $\tau_0 \sim 2.67\times 10^{-5}$ s is 2 orders of magnitude higher than that reported for cluster spin-glass systems (10^{-7}−10^{-10} s).[36] Figure 5d shows a linear fit of $T_f = T_0 - (E_a/k_B)[1/\ln(\nu/\nu_0)]$ which is a Vogel−Fulcher law, a modified Arrhenius relation,[34,37] where E_a is the energy barrier arising from the anisotropy and volume of the particle (in case of nanosystems), T_0 is the characteristic temperature, and k_B is the Boltzmann constant (8.617×10^{-5} eV·K^{-1}). The Vogel−Fulcher fit results are T_0 = (46.45 ± 0.36) K and E_a/k_B = (92.71 ± 1.82) K. Non-zero $T_0(<T_g)$ indicates cluster formation due to interacting spins. The relation $E_a/(k_BT_0) \gg 1$ indicates that the clusters are weakly coupled in the present alloy. A dimensionless Tholence parameter δT_{Th} (= $1 - T_0/T_f$) is used to classify the spin-glass systems of different origins such as short-range and strong RKKY (Ruderman−Kittel−Kasuya−Yosida) interactions.[38] δT_{Th} = 0.1 suggests the cluster-glass nature ($\delta T_{Th} \in [0.05, 0.5]$). Although τ_0 is relatively large, it can be deduced from the results of AC susceptibility that $MnNi_{0.7}Fe_{0.3}Ge$ behaves as a cluster spin-glass with weak coupling among the clusters, below 50 K.

Density Functional Calculations. To theoretically calculate the electronic structure and magnetic properties of the experimental $MnNi_{0.7}Fe_{0.3}Ge$ composition, a supercell comprising 4 f.u. was taken with 1 Ni ion substituted by Fe; this resulted in the very close composition $MnNi_{0.75}Fe_{0.25}Ge$. For this setup, the calculations were carried out for ferromagnetic and different antiferromagnetic configurations of the Mn and Fe magnetic moments. The ferromagnetic solution was found to be the most stable with the total energy

https://doi.org/10.1021/acsomega.2c01571
ACS Omega 2022, 7, 18110−18121

of −3235.1737 Ry per supercell. Other initial AFM configurations converged to the ferrimagnetic solution with 0.13 μ_B/f.u. and have a total energy 2.5 mRy (34 meV) higher.

This calculated FM ordering of the Mn and Fe magnetic moments has a total magnetic moment of 2.8 μ_B/f.u., including 2.7 and 2.9 μ_B per each of the two Mn ions, 0.8 μ_B/Fe, 0.1 μ_B/Ni, and −0.2 μ_B/Ge. The calculated FM total magnetic moment 2.8 μ_B/f.u. is very close to the saturation magnetic moment 2.6 μ_B/f.u. obtained from the experimental measurements reported above. In ref 39, we reported the calculated exchange interaction parameters for MnNiGe with the strong AFM nearest neighbor Mn ions J_{NN} = 705 K coupling between the Mn ions, much larger than the FM coupling J_{NN} = −302 K and AFM J_{NNN} = 67 K. In $MnNi_{0.7}Fe_{0.3}Ge$, due to the presence of Fe in the Ni positions, the FM coupling J_{NN} = −881 K between the Mn ions becomes large and dominates in the Mn subsystem over the AFM coupling J_{NN} = 299 K and J_{NNN} = 45 K. The moderate magnetic moment of the Fe ion causes much smaller values of the exchange coupling with the highest value between Fe and the nearest Mn ion as FM J_{NN} = −95 K. Thus, the FM and smaller AFM couplings among the Mn ions are determining the magnetic properties of $MnNi_{0.7}Fe_{0.3}Ge$.

In Figure 6, the first-principles electronic structure for $MnNi_{1-x}Fe_xGe$ (x = 0.25) is shown corresponding to the ferromagnetic arrangement of the Mn and Fe magnetic moments. The partial densities are plotted for the total and Fe-3d states on the highest panel, then the Mn and Ni-3d states, and finally, the Ge-4p and Ge-4s states. In the calculated total and partial densities of states (DOS), the strongly spin-polarized Mn-3d contribute from −5 to +5 eV with strong peaks near −2.8, −1.1, and +1.0 eV. Notice the two different types of the Mn ions (plotted as Mn and Mn1) due to the presence of Fe. The Ni and Ge ions also subdivided into two types; this difference in DOS and magnetic moments is negligible. The Ni states are almost nonmagnetic with deviating densities of states mostly below the Fermi energy (E_F) in both spin projections with the peaks from −5.0 to −0.5 eV below E_F. The selected $MnNi_{0.75}Fe_{0.25}Ge$ supercell is very close to the experimental composition. In order to check exact electronic concentration for Fe with x = 0.30, we added the rigid band approximation line in Figure 6, and it came very close to the Fermi energy and accounts for the 0.05 difference in x.

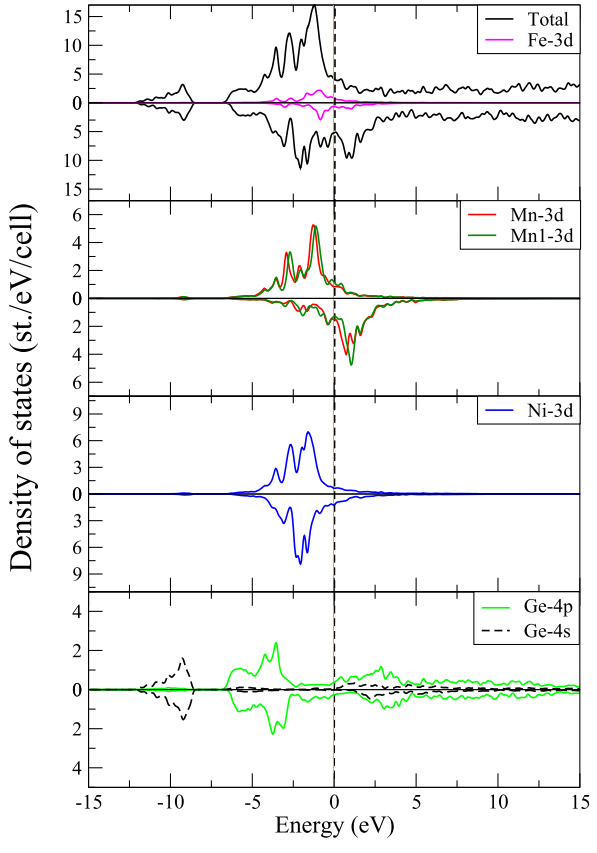

Figure 6. Calculated total and partial densities of states for $MnNi_{1-x}Fe_xGe$ (x = 0.25) given for two spin projections (↑ and ↓). The solid orange line close to the Fermi energy (E_F = 0 eV) corresponds to the rigid band shift for x = 0.30.

Specific Heat and Resistivity. Specific heat $C(T)$, measured in the presence of a few selected magnetic fields, is shown in Figure 7a. It exhibits two successive peaks at T_C and T_t which are in agreement with the magnetization data (see Table 1). The peak at T_C is broad and indicates a second-order phase transition from PM to FM, while a relatively sharp peak at T_t gives a hint of first-order phase transition. In addition, T_C gradually shifts toward high-T in applied magnetic fields, whereas T_t is found to be independent of H up to 5 kOe. Nevertheless, in higher fields (typically H > 5 kOe) $C(T_t)$ gets smeared out with a gradual shift of T_t toward high-T, implying a field-induced transition from a weak-AFM to FM state. This observation is in good agreement with a tiny/narrowed thermal hysteresis between FCC and FCW curves across T_t. Except for a strong FOPT, a tiny thermal hysteresis (weak-FOPT) cannot be traced out by heating and cooling curves of specific heat using commercial PPMS.[40] Zero-field C versus T is shown in the inset of Figure 7a. The data below 10 K is fit to the equation $C = \gamma_{el}T + \beta T^3$ to estimate the Sommerfeld parameter for the electronic contribution of specific heat (γ_{el}) and the Debye temperature (θ_D). Thus, obtained γ_{el} and $\theta_D = \sqrt[3]{1944p/\beta}$ (where p is the number of atoms in a formula unit) are (3.86 ± 0.1) mJ mol^{-1}·K^{-2} and (499 ± 5) K, respectively. γ_{el} indicates the metallic nature of the alloy and the density of states at the Fermi level [$D(E_F) = 3\gamma/(\pi^2 k_B^2 N_A)$] are found to be about 1.64 states/eV/f.u. The absence of a clear transition at T_f in $C(T)$ along with a frequency dependent cusp in $\chi_{AC}(T)$ indicates the glassy behavior.

$$\Delta S_{mag} = \int_0^{T'} \frac{C(H) - C(0)}{T}\, dT' \tag{7}$$

Figure 7d shows the temperature variation of magnetic entropy ΔS_{mag} (referred to MCE hereafter) which is estimated using eq 7. Conventionally, MCE is negative for a ferromagnet. For $MnNi_{0.7}Fe_{0.3}Ge$, MCE shows two dips, respectively, T_C and T_t. Negative MCE around T_t suggests the dominant ferromagnetic interactions in the alloy. An absolute MCE value at T_C, in an applied of 70 kOe, is found to be 0.5 J·kg^{-1}·K^{-1}.

$$|\Delta S_{mag}^{peak}| \sim H^n \tag{8a}$$

$$RCP \sim H^{1+1/\delta} \tag{8b}$$

$$n = 1 + \frac{1}{\delta}\left(1 - \frac{1}{\beta}\right) \tag{8c}$$

https://doi.org/10.1021/acsomega.2c01571
ACS Omega 2022, 7, 18110−18121

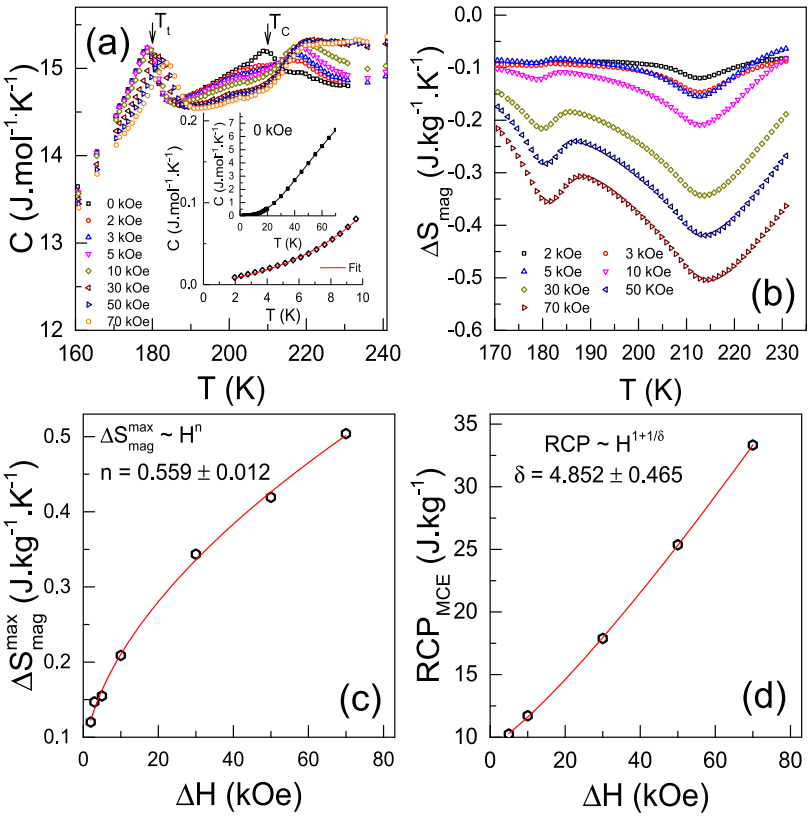

Figure 7. (a) Specific heat as a function of temperature from 160 to 240 K, measured in a few selected magnetic fields. T_C and T_t are shown by arrows. Inset: Zero-field data; a fit of $C(T) = \gamma_{el}T + \beta T^3$ below 10 K with $\gamma_{el} = (3.86 \pm 0.1)$ mJ mol^{-1}·K^{-2} and $\theta_D = (499 \pm 5)$ K and the specific heat data from 2 to 70 K. (b) Change in magnetic entropy under the effect of labeled magnetic fields. It is negative and exhibits two dips, respectively, at T_C and T_t. (c) Magnetic field dependence of ΔS^{max}_{mag} is fit to a power-law using eq 8a, yielding an exponent $n = 0.559 \pm 0.012$. (d) RCP versus magnetic field. A power-law fit using eq 8b yields an exponent $\delta = 4.852 \pm 0.465$.

Table 1. List of Transition Temperatures Inferred from the Temperature Dependence of Magnetization, Specific Heat, and Resistivity Data

temp	magnetization	specific heat	resistivity
T_C (K)	212	210	210
T_t (K)	180	178.5	180
T_f (K)	51.85	no feature	no feature

$$n = 1 + \left[\frac{\beta - 1}{\beta + \gamma}\right] \tag{8d}$$

Here, RCP is the relative cooling power defined as RCP = $\Delta S^{max}_{mag} \times \delta T_{FWHM}$. Though MCE and RCP values of $MnNi_{0.7}Fe_{0.3}Ge$ are not comparable to that of some of the prominent MCE materials,[41,42] magnetically distinct dual transitions (one at high-T) with a temperature difference of about 32 K can be tuned (by hydrostatic pressure or substitution) to achieve a table-like $\Delta S_{mag}(T)$. Parts c and d of Figure 7 show the field dependence of ΔS^{max}_{mag} and RCP, which are fit to the power-law dependences given in eqs 8a and 8b, respectively. The critical exponents, obtained from MCE plots using the relations given by eqs 8c and 8d,[43,44] are $\beta = 0.331 \pm 0.086$, $\gamma = 1.186 \pm 0.322$, and $\delta = 4.852 \pm 0.465$.

Figure 8a shows the temperature dependence of resistivity $\rho(T)$, measured in a few representative magnetic fields. The metallic character of the samples is evident from the positive slope of $\rho(T)$. As shown in the inset of Figure 8a, $d\rho/dT$ exhibits two peaks respectively at T_C and T_t which are in agreement with that of obtained from magnetization and specific heat (see Table 1). Magnetoresistance, MR = $[\rho(H) - \rho(0)]/\rho(0)$, is shown in Figure 8b. Under an applied field of 90 kOe, absolute MR is found to be about 6.0%. It is negative arising from the suppression of magnetic fluctuations by the application of field. The dip temperature T_d increases with application of magnetic fields, as expected for a ferromagnet. In addition, there is a minor kink at $T_t = 180$ K. Parts c and d of Figure 8 show the magnetic field variation of $|MR|^{max}$ and $|RCP|_{MR}$, respectively. A similar method, described to extract the exponents from MCE using eqs 8a and 8b, is followed. Thus, extracted critical exponents, $\beta = 0.392 \pm 0.130$, $\gamma = 1.779 \pm 0.672$, and $\delta = 5.545 \pm 1.239$, are in good agreement with those obtained MAP, KF, and magnetic entropy methods. For the sake of completeness, we have obtained an exponent α from resistivity. Considering the magnetic contributions, it has been theoretically proposed[45−52] and experimentally verified[53−56] that the temperature derivative of resistivity ($d\rho/dT$) and specific heat (C) exhibit similar temperature dependent behaviors in the critical region. Figure 9a shows zero-field $(1/\rho(T_C))(d\rho/dT)$ versus the t curve. A critical exponent α is extracted using a power-law given by eq 9[27]

$$\frac{1}{\rho(T_C)}\left(\frac{d\rho}{dT}\right) = \frac{A}{\alpha}[(t)^{-\alpha} - 1] + B \tag{9}$$

where A and B are constants, α is a critical exponent, and t is the reduced temperature. For the present alloy, the critical fit

https://doi.org/10.1021/acsomega.2c01571
ACS Omega 2022, 7, 18110−18121

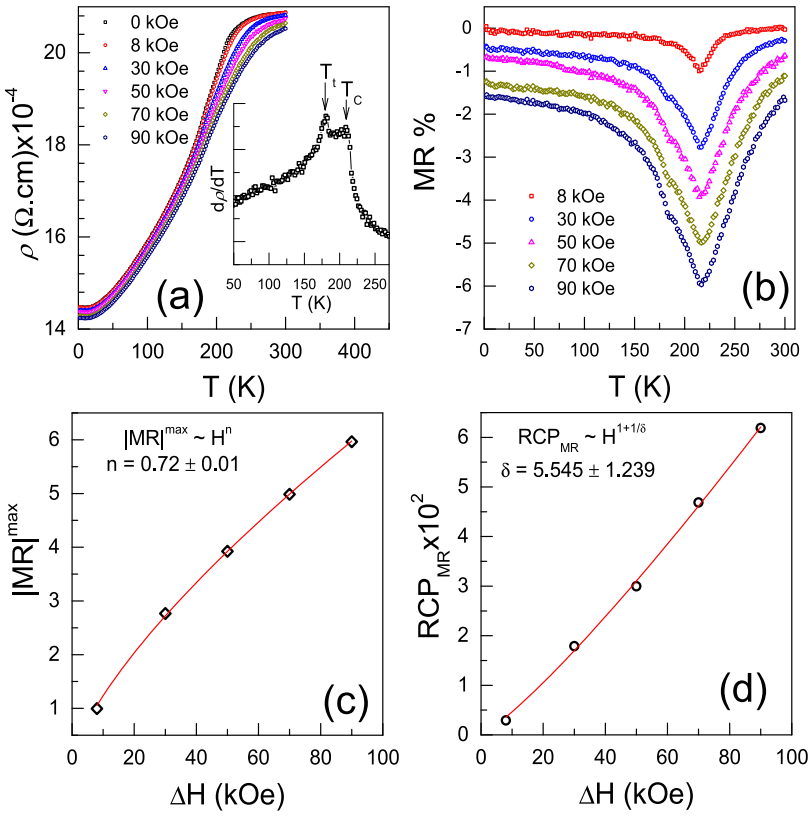

Figure 8. (a) Resistivity as a function of temperature, measured in labeled magnetic fields. It decreases with reduction in the temperature, revealing the metallic nature of $MnNi_{0.7}Fe_{0.3}Ge$. Inset shows the derivative $d\rho/dT$ which depicts two peaks corresponding to T_C and T_t. (b) Percentage of magnetoresistance. It is negative, indicating the suppression of magnetic fluctuations in external magnetic fields. In 90 kOe, MR is about 6.0%. (c) Maximum of absolute MR (taken from (b)) versus change in the magnetic field, ΔH. A power-law fit to the data yields an exponent $n = 0.72 \pm 0.01$. (d) Power-law fit of RCP_{MR} versus ΔH, yielding an exponent $\delta = 5.545 \pm 1.239$. The significance of the power-law fits is discussed in the text.

yields $\alpha = 0.55 \pm 0.05$. Positive α indicates the Ising type universality class, though it is larger about four times. α along with β and γ satisfies the universal scaling equation $\alpha + 2\beta + \gamma = 2$.[27] Experimentally obtained exponents α, β, and γ using modified Arrott plots, Kouvel Fisher, magnetocaloric, and magnetoresistance methods, listed in Table 2, are in good agreement within the error bars, establishing the self-consistency of the critical exponents.

Magnetic field variation of MR, measured at a few representative temperatures, is shown in Figure 9b. It is negative, as expected for a ferromagnetic metal, and isotropic against positive and negative applied fields. The absolute magnitude of MR increases as $T \rightarrow T_C$. MR is fit to a power-law dependence $MR \sim -H^m$.[57] A near quadratic dependence ($-H^{1.8}$) in the paramagnetic region (at 300 K) which indicates the suppression of spin fluctuations in the presence of magnetic fields.[58] Near the Curie temperature MR varies as $-H^{0.74}$. While further reducing the temperature below 20 K, MR is observed to follow near-linear dependence with $m = 0.92$. The isotropic (independent of magnetic field's direction) negative MR was attributed to the effect of spin alignment toward the interference contribution.[59] Later, Agrinskaya et al.[60] have attributed the observed unusual negative linear MR in narrow-band gap two-dimensional (2D) quantum well structures of GaAs-AlGaAs to the magnetic exchange interactions between localized and delocalized (thermally activated charge carriers) spins. For the present case, negative linear MR can be attributed to arise from the scattering of conduction electrons (s and p) from the itinerant d-electrons of constituent magnetic atoms.

In Figure 9c,d, the rescaled magnetic entropy and magnetoresistance are plotted against a reduced temperature θ

$$\theta = \left\{-\frac{T - T_p}{T_{cold} - T_p}\right\}, \quad T \leq T_p \tag{10a}$$

$$\theta = \left\{\frac{T - T_p}{T_{hot} - T_p}\right\}, \quad T > T_p \tag{10b}$$

where T_p is the temperature at which absolute ΔS_{mag} and MR are maximum and T_{cold} and T_{hot} are the hot and cold temperatures taken from the full width at half-maximum of ΔS_{mag} and |MR|. Overall, the data scale well by falling onto a single universal curve, irrespective of the strength of the applied magnetic field, inferring a second-order nature of the phase transition.[44,61] However, the curves are observed to deviate from the universal scaling below the structural transition T_t. Such a deviation from the scaling behavior is attributed to the first order phase transition below T_t.

SUMMARY

$MnNi_{0.7}Fe_{0.3}Ge$ alloy has been studied using the combined results of magnetization, specific heat, and resistivity along with electronic structure calculations. The alloy shows a ferromagnetic transition ($T_C \sim 212$ K) and an antiferromagnetic-like transition at ($T_t \sim 180$ K) followed by a spin-glass transition

https://doi.org/10.1021/acsomega.2c01571
ACS Omega 2022, 7, 18110−18121

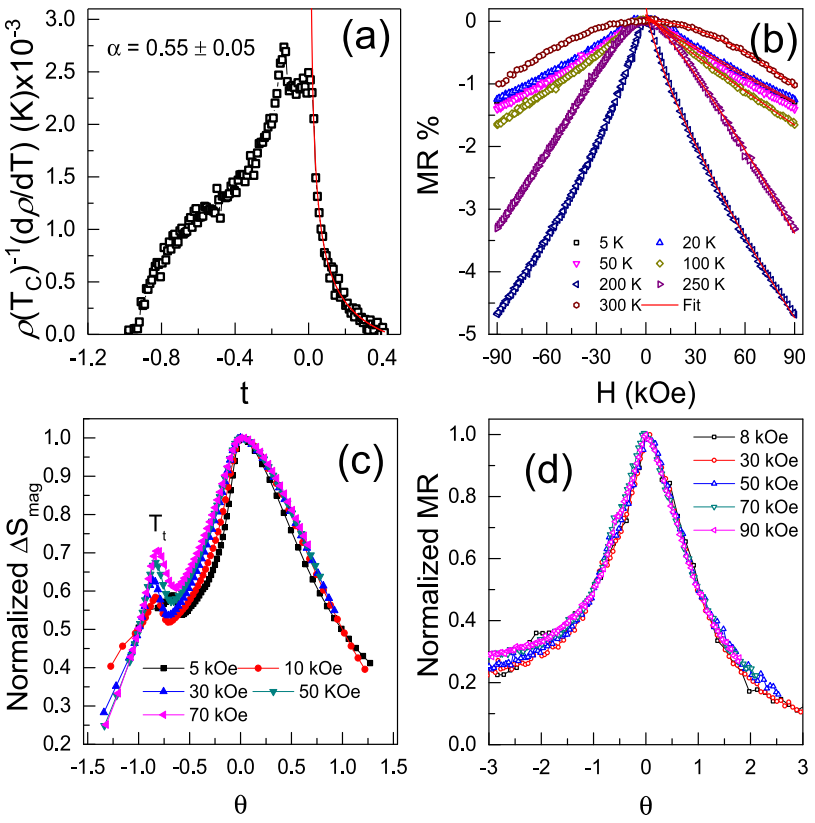

Figure 9. (a) Reduced temperature dependence of $(1/\rho(T_C)(d\rho/dT)$ in zero field. The data above critical temperature is fit (red solid line) to the eq 9, which yields a critical exponent $\alpha = 0.55 \pm 0.05$. (b) Magnetic field dependence of MR%. The curves are fit (red solid line) to the power-law MR $\propto -H^m$. A quadratic field dependence in the paramagnetic state suggests the suppression of spin fluctuations by applying external fields. As T approaches T_C, the magnitude of MR increases. Below T_C, a reduction in MR% with linear dependence on H is noticed. (c, d) Rescaled magnetic entropy and magnetoresistance against a reduced temperature θ. The data scales well by falling onto a single universal curve, irrespective of the strength of H, indicating a SOPT. However, the deviation from the universal scaling around T_t hints at a first-order phase transition.

Table 2. Critical Exponents of $MnNi_{0.7}Fe_{0.3}Ge$

method	T_C (K)	β	γ	δ	α	ref
modified Arrott Plot	212.51 ± 0.14	0.315 ± 0.076	1.327 ± 0.045	5.212 ± 1.162		this work
Kouvel-Fisher	212.45 ± 0.23	0.406 ± 0.002	1.293 ± 0.019	4.161 ± 0.062[a]		this work
critical isotherm	212.5			4.176 ± 0.011[a]		this work
magnetoresistance	∼213	0.392 ± 0.130	1.779 ± 0.672	5.545 ± 1.239	0.55 ± 0.05[b]	this work
magnetocaloric	∼213	0.331 ± 0.086	1.186 ± 0.322	4.852 ± 0.465		this work
mean-field theory		0.5	1.0	3.0	0.0	27
3D Heisenberg model		0.365	1.386	4.80	−0.0115	27
3D-Ising model		0.325	1.241	4.82	0.110	27
3D-XY model		0.346	1.316	4.81		27
tricritical model		0.25	1.0	5.0		27

[a] δ is obtained using Widom's relation $\delta = 1 + \gamma/\beta$. [b] α is extracted from the resistivity and specific heat using eq 9.

($T_g \sim 51.85$ K). Across T_C, (i) a well-scaled normalized magnetoresistance and magnetic-entropy, (ii) frequency independent hump in $\chi_{AC}(T)$, (iii) the critical exponents and $J(r) \sim r^{-4.75}$ suggest mixed (short and long-range) magnetic interactions with unclassified universality class of a second-order phase transition. Across T_t, the deviation from the scaling, a narrow thermal hysteresis between FCC and FCW, and relatively sharp transition in $C(T)$ and $1/\rho(d\rho/dT)$ indicate a weak first-order phase transition. Across T_g, the absence of a clear magnetic transition in $C(T)$ and the analysis of a frequency-dependent cusp in $\chi_{AC}(T)$ reveal cluster spin-glass behavior. Density functional calculations reveal mixed ferro- and antiferromagnetic interactions with the dominating ferromagnetic coupling, which is experimentally evident from the large positive Weiss temperature, magnetic saturation, and overall negative magnetic-entropy and magnetoresistance. The magnetically distinct dual transitions of $MnNi_{0.7}Fe_{0.3}Ge$ can be tuned to achieve large table-like MCE.

AUTHOR INFORMATION

Corresponding Author

S. Shanmukharao Samatham − *Department of Physics, Chaitanya Bharathi Institute of Technology, Hyderabad 500075, India;* orcid.org/0000-0002-1668-2304; Email: shanmukharao_physics@cbit.ac.in

https://doi.org/10.1021/acsomega.2c01571
ACS Omega 2022, 7, 18110−18121

Authors

Akhilesh Kumar Patel − *Magnetic Materials Laboratory, Department of Physics, Indian Institute of Technology Bombay, Mumbai 400 076, India*

Ashish Kumar Mishra − *UGC-DAE Consortium for Scientific Research, University Campus, Indore 452001 Madhya Pradesh, India*

Alexey V. Lukoyanov − *M. N. Miheev Institute of Metal Physics of Ural Branch of Russian Academy of Sciences, 620108 Ekaterinburg, Russia; Ural Federal University, 620002 Ekaterinburg, Russia;* orcid.org/0000-0003-4459-0893

Lyubov N. Gramateeva − *M. N. Miheev Institute of Metal Physics of Ural Branch of Russian Academy of Sciences, 620108 Ekaterinburg, Russia*

Archana Lakhani − *UGC-DAE Consortium for Scientific Research, University Campus, Indore 452001 Madhya Pradesh, India*

Ganesan Vedachalaiyer − *Medi-Caps University, Indore 453331 Madhya Pradesh, India; UGC-DAE Consortium for Scientific Research, University Campus, Indore 452001 Madhya Pradesh, India*

Suresh Krishnawarrier Gopinatha Warrier − *Magnetic Materials Laboratory, Department of Physics, Indian Institute of Technology Bombay, Mumbai 400 076, India*

Complete contact information is available at: https://pubs.acs.org/10.1021/acsomega.2c01571

Author Contributions

[#]Part of the work was carried out while in service at MVGR College of Engineering, Vizianagaram 535005, A.P., India.

Notes

The authors declare no competing financial interest.

■ ACKNOWLEDGMENTS

S.S.S., A.K.P., and K.G.S. thank IRCC and the Department of Physics, IIT Bombay, for X-ray diffraction and magnetization facilities. S.S.S. acknowledges UGC-DAE CSR, Indore, for financial support under the Collaborative Research Scheme (CSR-IC-256/2017-18/1337). V.G. acknowledges UGC-DAE CSR, Indore, for the support. A.K.M. thanks CSIR, India, for SRF [File No.: 09/926(0011)2K18]. K.G.S. acknowledges financial support through Indo-Russian project: DST/INT/RFBR/IDIR/P-01/2016. The theoretical studies are supported by the Russian Science Foundation (Project No. 22-42-02021) for the electronic structure calculations and Ministry of Science and Higher Education of the Russian Federation for the exchange parameters calculations (theme "Electron" No. AAAA-A18-118020190098-5).

■ REFERENCES

(1) Liu, Z. K.; Yang, L. X.; Wu, S.-C.; Shekhar, C.; Jiang, J.; Yang, H. F.; Zhang, Y.; Mo, S.-K.; Hussain, Z.; Yan, B.; Felser, C.; Chen, Y. L. Observation of unusual topological surface states in half-Heusler compounds LnPtBi (Ln = Lu, Y). *Nat. Commun.* **2016**, *7*, 1−7.

(2) Yang, H.; Yu, J.; Parkin, S. S. P.; Felser, C.; Liu, C.-X.; Yan, B. Prediction of Triple Point Fermions in Simple Half-Heusler Topological Insulators. *Phys. Rev. Lett.* **2017**, *119*, 136401.

(3) Yan, B.; Felser, C. Topological Materials: Weyl Semimetals. *Annu. Rev. Condens. Matter Phys.* **2017**, *8*, 337.

(4) Wang, X.; Cheng, Z.; Wang, J.; Wang, X.-L.; Liu, G. Recent advances in the Heusler based spin-gapless semiconductors. *J. Mater. Chem. C* **2016**, *4*, 7176.

(5) Kainuma, R.; Imano, Y.; Ito, W.; Sutou, Y.; Morito, H.; Okamoto, S.; Kitakami, O.; Oikawa, K.; Fujita, A.; Kanomata, T.; Ishida, K. Magnetic-field-induced shape recovery by reverse phase transformation. *Nature* **2006**, *439*, 957.

(6) Chmielus, M.; Zhang, X. X.; Witherspoon, C.; Dunand, D. C.; Müllner, P. Giant magnetic-field-induced strains in polycrystalline Ni−Mn−Ga foams. *Nat. Mater.* **2009**, *8*, 863.

(7) Balke, B.; Fecher, G. H.; Kandpal, H. C.; Felser, C.; Kobayashi, K.; Ikenaga, E.; Kim, J.-J.; Ueda, S. Properties of the quaternary half-metal-type Heusler alloy $Co_2Mn_{1-x}Fe_xSi$. *Phys. Rev. B* **2006**, *74*, 104405.

(8) Shigeta, I.; Fujimoto, Y.; Ooka, R.; Nishisako, Y.; Tsujikawa, M.; Umetsu, R. Y.; Nomura, A.; Yubuta, K.; Miura, Y.; Kanomata, T.; Shirai, M.; Gouchi, J.; Uwatoko, Y.; Hiroi, M. Pressure effect on the magnetic properties of the half-metallic Heusler alloy Co_2TiSn. *Phys. Rev. B* **2018**, *97*, 104414.

(9) Sattar, M. A.; Ahmad, S. A.; Hussain, F.; Cazorla, C. First-principles prediction of magnetically ordered half-metals above room temperature. *Journal of Materiomics* **2019**, *5*, 404.

(10) Khovaylo, V. V.; Skokov, K. P.; Gutfleisch, O.; Miki, H.; Takagi, T.; Kanomata, T.; Koledov, V. V.; Shavrov, V. G.; Wang, G.; Palacios, E.; Bartolomé, J.; Burriel, R. Peculiarities of the magnetocaloric properties in Ni-Mn-Sn ferromagnetic shape memory alloys. *Phys. Rev. B* **2010**, *81*, 214406.

(11) Liu, J.; Gottschall, T.; Skokov, K. P.; Moore, J. D.; Gutfleisch, O. Giant magnetocaloric effect driven by structural transitions. *Nat. Mater.* **2012**, *11*, 620.

(12) Liu, E.; Wang, W.; Feng, L.; Zhu, W.; Li, G.; Chen, J.; Zhang, H.; Wu, G.; Jiang, C.; Xu, H.; de Boer, F. Stable magnetostructural coupling with tunable magnetoresponsive effects in hexagonal ferromagnets. *Nat. Commun.* **2012**, *3*, 873.

(13) Xu, K.; Li, Z.; Liu, E.; Zhou, H.; Zhang, Y.; Jing, C. Magnetocaloric effect and negative thermal expansion in hexagonal Fe doped MnNiGe compounds with a magnetoelastic AFM-FM-like transition. *Sci. Rep.* **2017**, *7*, 41675.

(14) Bażela, W.; Szytula, A.; Todorović, J.; Tomkowicz, Z.; Zieba, A. Crystal and magnetic structure of NiMnGe. *Phys. Status Solidi (a)* **1976**, *38*, 721.

(15) Fjellvåg, H.; Andresen, A. On the crystal structure and magnetic properties of MnNiGe. *J. Magn. Magn. Mater.* **1985**, *50*, 291.

(16) Wang, C.; Hu, Y.; Hu, Q.; Chen, F.; Zhang, M.; He, X.; Li, Z.; Wang, D.; Cao, Q.; Du, Y. Successive magnetic phase transitions and magnetocaloric effect in the MnNiFeGe alloy. *J. Magn. Magn. Mater.* **2017**, *439*, 13.

(17) Giannozzi, P.; et al. QUANTUM ESPRESSO: a modular and open-source software project for quantum simulations of materials. *J. Phys.: Condens. Matter* **2009**, *21*, 395502.

(18) Rodríguez-Carvajal, J. Recent advances in magnetic structure determination by neutron powder diffraction. *Physica B* **1993**, *192*, 55−69.

(19) Momma, K.; Izumi, F. VESTAâĂŘ3 for three-dimensional visualization of crystal, volumetric and morphology data. *J. Appl. Crystallogr.* **2011**, *44*, 1272.

(20) Rhodes, P.; Wohlfarth, E. P.; Jones, H. The effective Curie-Weiss constant of ferromagnetic metals and alloys. *Proceedings of the Royal Society of London. Series A. Mathematical and Physical Sciences* **1963**, *273*, 247.

(21) Wohlfarth, E. P. Magnetic properties of crystallineand amorphous alloys: A systematic discussion based on the Rhodes-Wohlfarth plot. *J. Magn. Magn. Mater.* **1978**, *7*, 113.

(22) Fisher, M. E. The theory of equilibrium critical phenomena. *Rep. Prog. Phys.* **1967**, *30*, 615.

(23) Stanley, H. E. *Introduction to Phase Transitions and Critical Phenomena*; Oxford University Press: New York, 1971.

(24) Arrott, A. Criterion for Ferromagnetism from Observations of Magnetic Isotherms. *Phys. Rev.* **1957**, *108*, 1394.

(25) Banerjee, B. K. On a generalised approach to first and second order magnetic transition. *Phys. Lett.* **1964**, *12*, 16.

(26) Arrott, A.; Noakes, J. E. Approximate Equation of State For Nickel Near its Critical Temperature. *Phys. Rev. Lett.* **1967**, *19*, 786.
(27) Kaul, S. N. Static critical phenomena in ferromagnets with quenched disorder. *J. Magn. Magn. Mater.* **1985**, *53*, 5.
(28) Huang, K. *Statistical Mechanics*, 2nd ed.; Wiley: New York, 1987.
(29) Widom, B. Degree of the Critical Isotherm. *J. Chem. Phys.* **1964**, *41*, 1633.
(30) Widom, B. Equation of State in the Neighborhood of the Critical Point. *J. Chem. Phys.* **1965**, *43*, 3898.
(31) Fisher, M. E.; Ma, S.-k.; Nickel, B. G. Critical Exponents for Long-Range Interactions. *Phys. Rev. Lett.* **1972**, *29*, 917.
(32) Pinninti, S.; Raju, G. J. N. Critical behaviour and magneto-caloric properties of hexagonal $MnCo_{0.7}Fe_{0.3}Ge$. *Mater. Res. Express* **2019**, *6*, 116563.
(33) Pinninti, S.; Sarita, P.; Raju, G. J. N. Magnetocaloric effect near room temperature and critical behaviour of Fe doped $MnCo_{0.7}Fe_{0.3}Ge$. *Solid State Commun.* **2021**, *327*, 114211.
(34) Mydosh, J. A. *Spin Glasses: An Experimental Introduction*; Taylor and Francis: London, 1993.
(35) Binder, K.; Young, A. P. Spin glasses: Experimental facts, theoretical concepts, and open questions. *Rev. Mod. Phys.* **1986**, *58*, 801−976.
(36) Bontemps, N.; Rajchenbach, J.; Chamberlin, R. V.; Orbach, R. Dynamic scaling in the $Eu_{0.4}$ $Sr_{0.6}S$ spin-glass. *Phys. Rev. B* **1984**, *30*, 6514.
(37) Souletie, J.; Tholence, J. L. Critical slowing down in spin glasses and other glasses: Fulcher versus power law. *Phys. Rev. B* **1985**, *32*, 516.
(38) Tholence, J.-L. Recent experiments about the spin-glass transition. *Physica B* **1984**, *126*, 157.
(39) Samatham, S. S.; Patel, A. K.; Lukoyanov, A. V.; Suresh, K. G. Revelation of spin glass behavior in Ru doped MnNiGe: experiment and theory. *J. Phys.: Condens. Matter* **2019**, *31*, 125803.
(40) Lashley, J. C.; et al. Critical examination of heat capacity measurements made on a Quantum Design physical property measurement system. *Cryogenics* **2003**, *43*, 369.
(41) GschneidnerJr, K. A., Jr.; Pecharsky, V. K.; Tsokol, A. O. Recent developments in magnetocaloric materials. *Rep. Prog. Phys.* **2005**, *68*, 1479.
(42) Franco, V.; Blázquez, J. S.; Ingale, B.; Conde, A. The Magnetocaloric Effect and Magnetic Refrigeration Near Room Temperature: Materials and Models. *Annu. Rev. Mater. Res.* **2012**, *42*, 305.
(43) Franco, V.; Blazquez, J. S.; Conde, A. Field dependence of the magnetocaloric effect in materials with a second order phase transition: A master curve for the magnetic entropy change. *Appl. Phys. Lett.* **2006**, *89*, 222512.
(44) Franco, V.; Conde, A.; Romero-Enrique, J. M.; Blazquez, J. S. A universal curve for the magnetocaloric effect: an analysis based on scaling relations. *J. Phys.: Condens. Matter* **2008**, *20*, 285207.
(45) Mannari, I. Anomaly in electrical resistivity of ferromagnetic metals near T_C. *Phys. Lett. A* **1968**, *26*, 134.
(46) Fisher, M. E.; Langer, J. S. Resistive Anomalies at Magnetic Critical Points. *Phys. Rev. Lett.* **1968**, *20*, 665.
(47) Takada, S. Resistive Anomalies at Magnetic Critical Points. *Prog. Theor. Phys.* **1971**, *46*, 15.
(48) Kasuya, T.; Kondo, A. Anomalous resistivity near curie temperature due to the critical scattering. *Solid State Commun.* **1974**, *14*, 253.
(49) Geldart, D. J. W.; Richard, T. G. Theory of spin-fluctuation resistivity near the critical point of ferromagnets. *Phys. Rev. B* **1975**, *12*, 5175.
(50) Richard, T. G.; Geldart, D. J. W. Theory of spin-fluctuation resistivity near the critical point of binary alloys and antiferromagnets. *Phys. Rev. B* **1977**, *15*, 1502.
(51) Alexander, S.; Helman, J. S.; Balberg, I. Critical behavior of the electrical resistivity in magnetic systems. *Phys. Rev. B* **1976**, *13*, 304.
(52) Balberg, I.; Helman, J. S. Critical behavior of the resistivity in magnetic systems. II. Below T_c and in the presence of a magnetic field. *Phys. Rev. B* **1978**, *18*, 303.
(53) Zumsteg, F. C.; Parks, R. D. Electrical Resistivity of Nickel Near the Curie Point. *Phys. Rev. Lett.* **1970**, *24*, 520.
(54) Simons, D. S.; Salamon, M. B. Specific Heat and Resistivity Near the Order-Disorder Transition in β-Brass. *Phys. Rev. Lett.* **1971**, *26*, 750.
(55) Simons, D. S.; Salamon, M. B. Specific heat and resistivity of gadolinium near the Curie point in external magnetic fields. *Phys. Rev. B* **1974**, *10*, 4680.
(56) Shacklette, L. W. Specific heat and resistivity of iron near its Curie point. *Phys. Rev. B* **1974**, *9*, 3789.
(57) Nath, T. K.; Majumdar, A. K. Magnetoresistance and its correlation with magnetization in γ-$Fe_{80-x}Ni_xCr_{20}$ ($14 < \sim x < \sim 30$) alloys near the multicritical point. *Phys. Rev. B* **1998**, *57*, 10655.
(58) Pippard, A. B. *Magnetoresistance in Metals*; Cambridge University Press: Cambridge, 1989.
(59) Ioffe, L. B.; Spivak, B. Z. Giant magnetoresistance in the variable-range hopping regime. *J. Exp. Theor. Phys.* **2013**, *117*, 551.
(60) Agrinskaya, N. V.; Kozub, V. I.; Mikhailin, N. Y.; Shamshur, D. V. Spin-controlled negative magnetoresistance resulting from exchange interactions. *JEPT Lett.* **2017**, *105*, 484.
(61) Samatham, S. S.; Ganesan, V. Critical behavior, universal magnetocaloric, and magnetoresistance scaling of MnSi. *Phys. Rev. B* **2017**, *95*, 115118.

https://doi.org/10.1021/acsomega.2c01571
ACS Omega 2022, 7, 18110−18121